Analysis of an Innovative Inward Turning Inlet with Hydrocarbon Fuel at Mach 7

Faure J. Malo-Molina
Datta V. Gaitonde
Paul H. Kutschenreuter
AFRL/VAAC-VAAI
Wright-Patterson AFB, OH *45433-7913*

and

Houshang B. Ebrahimi
Aerospace Testing Alliance, Inc., AEDC
Arnold AFB, TN 37389

Abstract

Two different strategies, one based on a new innovative elliptic design and the other based on a classic non-axisymetric or rectangular cross-section, are explored numerically. Both configurations utilize the same dual-compression strategy – the first in the pitch plane, followed by the second in the yaw plane and the compression ratio is maintained at similar values. Particular emphasis is placed on understanding the fully three-dimensional viscous/inviscid interaction phenomena encountered, and their impact on distortion is analyzed. This radical inlet design is compared with respect to phenomenological models of performance. Both configurations are followed by an analogous combustor containing a commonly used trap vortex combustor (TVC) or cavity. The chosen flight trajectory is taken at *Mach 7* and a dynamic pressure of *1500 psf*.

The elliptic cross-section inlet, denoted "Jaws" because of its shape, is designed using compression theory to provide planar shocks emanating from the leading edges. Advantages over the rectangular-duct or base design include an absence of shock-on-cowl-lip interactions – which can lead to catastrophic failure of the cowl-lip – and potentially lower losses through viscous-inviscid interactions. Additional effects at the side edges of the base line design, where captured mass flow of air escapes behind the first set of shocks, are analyzed. And finally, a considerable reduction is found in the boundary layer growth and higher combustion efficiency in Jaws than its rectangular counterpart.

Introduction

Since the late 1950s, many efforts to develop practical hypersonic flight and associated technologies have been ongoing.[i,ii] During this time, substantial advancements have been made in lightweight, high temperature structural materials and thermal protection systems; rocket, turbine, ramjet and scramjet propulsion; computational fluid dynamics and structural analysis; and multidisciplinary optimization. Taken together, these technologies are ever closer to helping realize practical, long-range hypersonic transport and routine, affordable space access.

The advantages of supersonic combustion devices for high-speed propulsion are well known[iii] and a number of recent theoretical, experimental and numerical efforts have proposed and examined various

designs. Despite advances in scramjet analysis, many uncertainties persist about three-dimensional, supersonic chemically reacting flows, and significant challenges need to be overcome, including high heat loads and low combustion efficiency arising from inefficient mixing at high-speeds.[iv] Simulation methods can complement difficult to perform experiments and thus play a major role in developing a comprehensive understanding of the key phenomena that determine performance.

This paper describes a numerical effort to explore a new hypersonic turning inlet (denoted "Jaws" because of its general appearance) that may improve the properties of the internal flowpath, by modifying shock -boundary layer and shock-shock interactions that affect the overall efficiency of the engine.[v] Although many variants of scramjet configurations have been proposed, this paper compares the new prototype with a basic rectangular inlet similar to one previously analyzed by the authors[vi], with emphasis on drag forces and flow characteristics. Both designs are well-suited to explore the generic three-dimensional fluid dynamic features likely to be encountered in a scramjet but isolated from the overwhelming geometrical complexity of an actual device. In addition, the paper looks into the effects due to combustion of a reacting stoichiometric fuel-air mixture with emphasis on the kinematics and dynamics of complex structures that result from interactions between shocks, chemical reactions and the expansion in the nozzle which ultimately yields thrust.

In the last few years, wall cavities have gained the attention of the scramjet community as a promising flame-holding device, owing to results obtained in flight tests and to feasibility demonstrations in laboratory scale supersonic combustors. However, comprehensive studies are needed to determine the optimal configuration which will yield the most effective performance. Numerous geometries have been tested to improve the mixing characteristics of fuel injection ports during the NASP program and in recent years. One interesting concept initiates detonation with supersonic jets recessed in a small cavity. By focusing these towards the center of the cavity, a region of high energy density can be produced to cause onset of detonation. The enhanced pressures and temperatures within the volume of the cavity result in fast turbulent mixing.

In some cases the intrusive fuel injectors and flame-holders are difficult to maintain inside the extremely harsh environment of a scramjet combustor and often yield very complex features with severe internal drag penalties. In addition, external ignition aids are commonly employed at low flight Mach numbers (i.e., around M = 4) and may require scramjet-based systems to carry potentially heavy generators. These devices reduce available payload for fuel at the low speed takeover point. These techniques include flush-wall fuel injection, wall-mounted flame holding, and devices to enhance the atomization and vaporization characteristics of liquid fuels. Significant attention has been paid to analyzing combustor performance using a wide array of conventional and advanced diagnostic techniques. Plasma igniters also hold promise for future supersonic combustion applications. With their ability to produce combustion-enhancing radicals at relatively low power and their robust performance, they are ideal candidates to overcome many of the obstacles faced in scramjet combustor design.

This work considers a fuel injector and flame-holder concept that incorporates flush wall fuel injection upstream of a wall cavity. Figure 1 depicts both scramjet configurations considered in the present study. The design is comprised of a dual-plane compression inlet system followed by a constant-area combustor and a short 15˚ expansion nozzle. Since this study is focused principally on the inlet and combustor, the nozzle is truncated. The simplified design is well-suited to explore the generic three-dimensional features likely to be encountered in a scramjet but isolated from the overwhelming geometrical complexity of an actual device.
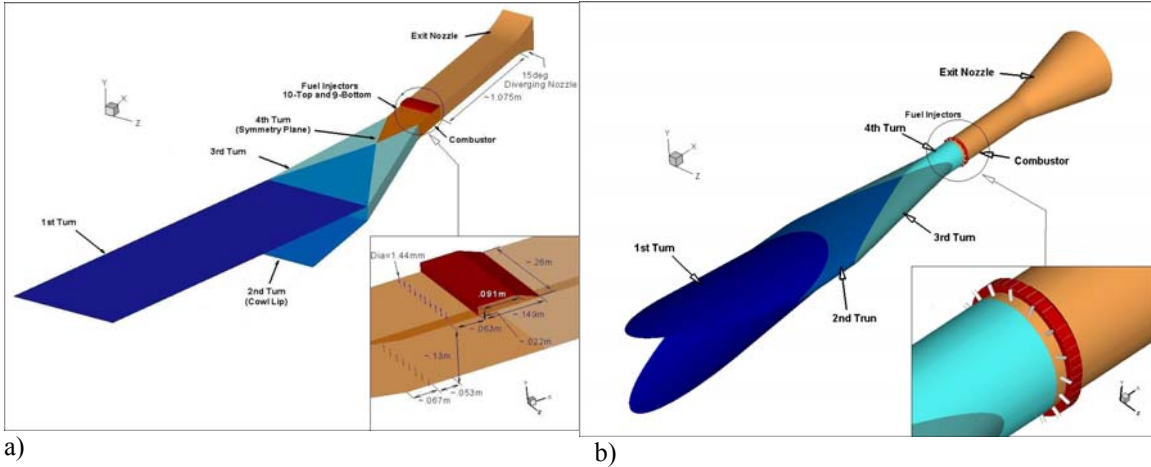
Fig. 1: Picture of the full scramjet engine configuration and a close up of its burner/combustor section for a) the baseline design and b) Jaws.

Analysis

Figure 2 shows the computational domains. A structured mesh is employed to analyze the region of interest. The rectangular scramjet is symmetric about the vertical XY-plane, and thus only half of the scramjet is computed using a structured mesh. The Jaws grid is symmetrical about the vertical XY- and horizontal XZ-plane. Wherever possible, vertical and/or horizontal symmetry is invoked to minimize the computational effort. The computational domains for both geometries were divided into sixteen zones: five zones for each of the inlet ramps, one for the combustor and exit-nozzle, one for the cavity and the others for the injectors. At the inlets alone, the grids have about 1.5 million points with clustering being employed near the walls to resolve the boundary layers and viscous/inviscid interactions (see Figure 2a-b). The grids used for the combustor section have about 1 million points (see Figure 2c).
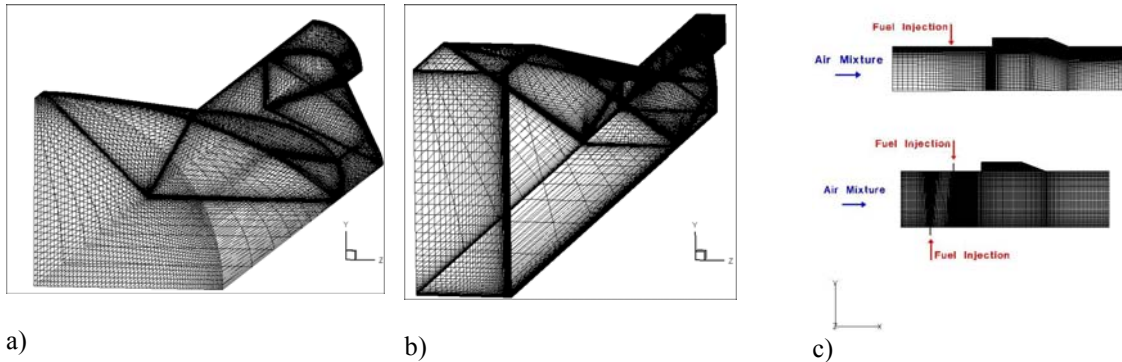

Figure 2: Grid structures: a) Jaws, b) Rectangular inlet, and c) combustor configurations for the turning inlets (top-Jaws and bottom rectangular inlet).

The grid indices (i, j and k) are generally oriented in the streamwise (x), vertical (y) and spanwise (z) axes respectively as shown above. Both geometries were initially simulated without viscous effects to match basic design characteristics; for this the Euler equations were employed. A standard central second-order scheme is employed for the viscous fluxes. After finalizing the design, subsequent cases were analyzed with the full 3-D steady Navier-Stokes equations together with a k-w model[vii] without body forces or external heat addition. The spatial accuracy used for all calculations was 2nd order, with a Gauss-Seidel iterative matrix solution scheme.

As noted earlier, both configurations are topologically equivalent and operate through successive pitch and yaw compressions. Ramps in both geometries are inclined at 9° to the freestream, yielding similar planar shocks initially from the upper and lower surfaces and subsequently from the sidewall

compressions. The boundary conditions were: freestream at the front entrance of the inlets, adiabatic/non-slip at the walls, sink at the back exit plane, and slip wall for the exterior sides of the entrance as well as the symmetry planes.

Using a slip wall condition at the exterior sides of the rectangular inlet is somewhat inaccurate. This condition can be only exploited when this section of the inlet is grouped into a series of similar inlets next to each other (side-to-side). Otherwise, air leak behind the first two shock interactions due to the static pressure differential between the outside (freestream) and the flow captured in the inlet. For the rectangular inlet configuration, this makes the first set of shocks interact differently. The first set of shocks becomes non-planar (rounded boundaries), exposing the cowl lip and lower sections of the second ramp to have a greater stagnation area and higher heating loads. The Jaws design has an advantage: the first shock interacts with the first ramp and follows the lips of its entrance, eliminating or rendering very insignificant the leakage when flying near $\alpha=\beta=0º$.

The throat area of the rectangular inlet has a width equal to twice the throat height. Both inlets have the same area contraction ratio of 11.1. For the rectangular inlet, the fuselage ramp has an initial height of 1.8ft *(0.54864 m)* that terminates at the point where the pitch-plane shock from the ramp reflects off the cowl-lip, at which station sidewalls are assumed to start. The sidewalls of the inlet are inclined at equal angle to the free-stream. The resulting span-wise shock waves (refer to Fig. 3a; third and fourth shocks) facilitate the evolution of a highly three-dimensional flow at the entrance of a constant-area duct representing the isolator/combustor segment,[viii] which starts where the crossing shocks (from inviscid estimates) reach the opposite walls.

In Jaws, on the other hand, the designed pitch- and yaw-plane shocks (denoted first and third) reflect off each other, while the second and fourth shocks reflect from the walls as seen in Fig. 3b. The inlet ramp has an initial height of 3ft *(0.9144 m)* from the leading edge of the upper lip to the lower one. The section after the fourth turning is equal in length to the throat radius of Jaws for both inlets ($(^2/_\Pi)^{1/2}$ times the throat height of the rectangular design). The throat areas at the back ends are equal to each other.

The free-stream conditions chosen are Mach 7, 1,500 psf *(71.82 kPa)* dynamic pressure corresponding to 43.7 psf *(2.09 kPa)* static pressure and a fixed temperature at 400.8 R$^\circ$ *(222.67 C$^\circ$)*. Two different cases are examined for each turning inlet configuration section. The first case is to provide an understanding of the internal flow without viscous effects and describe the planar shocks and shock-shock interactions in the designs. The second case is analyzed with a turbulence model. And finally, a third set of cases will be done for the combustor sections independently from the front sections of their compression inlets (see Table 1). For the combustor analysis the inlet exit results were averaged and assumed to enter the combustor uniformly.

Table 1: Description of all cases analyzed for a: Rectangular and b: Jaws inlets.			
Cases	Engine Section	Pitch/Yaw (degree)	Flow Type
1 $_{a,b}$	Inlet	0	Inviscid
2 $_{a,b}$	Inlet	0	Turbulent
3 $_{a,b}$	Combustor/nozzle	0	Turbulent

Inviscid Results (Case 1$_{a-b}$)

The shock structure for Cases 1a and b are shown in Figures 3a-b respectively. The structures are clearly planar as designed, even with the curvature of the inward turning inlet surface. Aspects of the solution along the centerline for the tubular inward turning inlet are shown for comparison in Fig. 7. The traces of various shocks are clearly evident in the jumps observed. The Mach number drops from 7 to slightly above 4.5 after the first shock pair (since this reflects the point of reflection on the symmetry plane). A further reduction is observed after the second reflection towards the isolator to about 2.8.

A troubling revelation obtained from the computations is the occurrence of separation whose effect on the downstream segment of the domain is seen in Figure 3b, where the cross-sectional distribution

of Mach number is plotted in the inset. It is evident that the distribution of Mach numbers is not uniform, with regions of lower values extending into the flow at the upper and lower edges, as well as the sides. These are effects of separation occurring upstream, due to shock boundary layer interactions, similar to those documented earlier for the rectangular inlet configuration.[ix] These phenomena typically degrade the performance of the inlet by increasing the distortion of the flow at the entrance to the combustor.
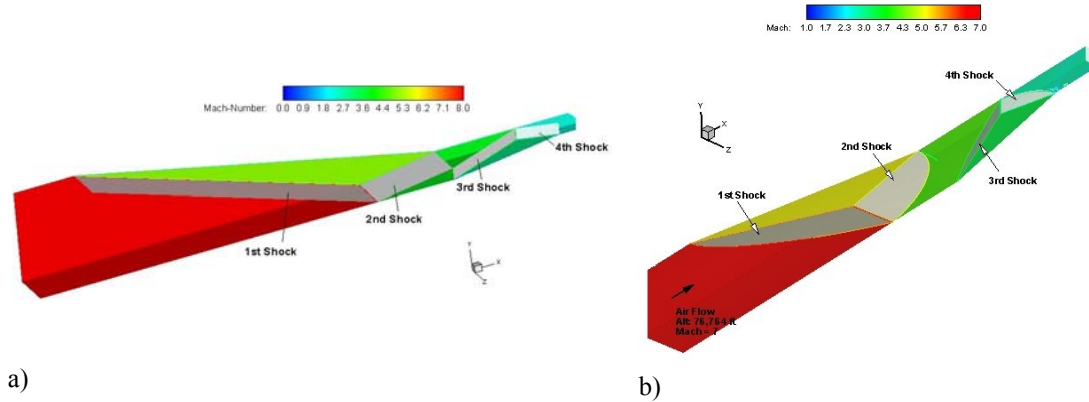

a)

b)

Figure 3: Shock structure in anterior segment of design and Mach number contours for a) Rectangular and b) Jaws inlet.

Inlets Viscous Results (Cases 2$_{a-b}$)

The Rectangular inlet design follows to some extent that described by Gaitonde,[1] but with some key differences. First, the inlet angle is increased in this work so that the nominal Mach number, from inviscid estimates, is roughly 2 at the entrance of the combustor. In Ref. ix, a smaller compression is utilized to explore MHD-assisted compression. Second, since the inlet and combustor are the main focus of this effort, the nozzle flow is not of particular interest and is therefore truncated from that utilized in Ref. i. For this section of the inlets was simulated with the GASP code, and since the temperature is relatively low in the nozzle, chemical reactions were not considered. The Roe flux-difference scheme was employed, together with the min-mod limiter. Fine-scale effects of turbulence were simulated with Menter's *k-w* SST model. These inlet calculations were then employed to extract the average conditions at the entrance to the combustor.

Figure 4 depicts the turbulent flow structure for the rectangular inlet configuration through several Mach number contours at the symmetry plane (k_{min}), an XZ-Plane located 0.01ft *(3 mm)* away from the boundary layer at the bottom surface of the inlet and six other YZ-planes of interest. The oblique shock wave caused by the first compression ramp follows the expected path or estimated location as seen in Fig. 3a. This shock bounces off the cowl lip (Station II in Fig. 4) and impinges on the top boundary where the boundary layer exhibits a significant thickening as a result. At this location, the sidewalls converge to produce a swept shock system to yield a highly three-dimensional flow (Station III in Fig. 4). Further into the inlet two shocks (3rd and 4th, as initially shown in Fig. 3a) cross in a non planar manner at the symmetry XY-Plane (see Station IV in Fig. 4) causing the 4th shock to considerably shift position from the initially predicted calculation (Euler solution, see Fig. 3a); the inset in Figure 4 shows the result of this complex interaction. Finally, the 4th shock impacts the side walls at 0.025m (see Station V in Fig. 4) upstream from the inviscid design at the straight section into the combustor. This effect adversely impacts performance of the inlet through pressure distortion and drag caused by the premature contraction. As shown in the close-up at the right bottom corner of Fig. 4, the flow turns and expands around the 4th corner producing a recirculation flow. From this inlet calculation at the i_{max} plane (see Station VI in Fig. 4), the boundary layer profiles and all other variables may employed to provide an initial condition for the flow entering the combustor.
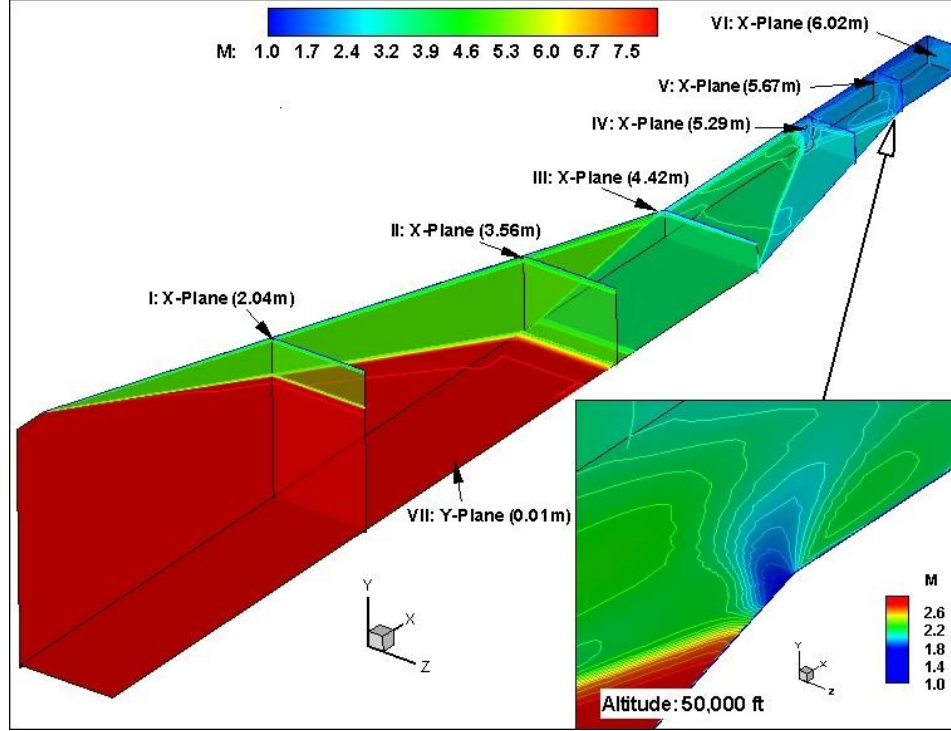
Figure 4: Mach contours illustrate aspects of viscous shock-to-shock and – boundary layer interactions in the rectangular inlet.

This analysis suggests that shock boundary layer interactions have a profound impact on the flow exiting the inlet. These non-ideal effects are amplified with distance downstream, with the result that a shock/boundary layer interaction occurs downstream of the corner. When separation occurs in this context, there is a potential for a weak-interaction limit to be reached, for choking to occur downstream and possible degradation of isolator performance. This turbulence solution suggests avenues for redesign by altering lengths to accommodate for the viscous effects, which is being explored in ongoing research. Another possibility is interaction control through porous wall effects, which will be explored in subsequent efforts.

Further details are exhibited in Figures 5a, showing Mach (top) and total pressure (bottom) contours at the symmetry plane (y_{min}), and Fig. 5b shows the irregularities of the flow at the exit section of the inlet on the 4th turn for different variables. At this location (see Station V in Fig. 4 as reference), four different parameters are employed as follows: 1) mass average Mach number or Mach-mass flow rate per unit area over the average mass flow rate, 2) thrust per unit area, 3) mass flow rate and 4) Mach number contours (see Equations 1 to 4).

$$Eq.1: M\_massflow = \int (\rho u_x M)dA = \int \rho^{3/2} u_x \left(\frac{\left(u_x{}^2 + u_y{}^2 + u_z{}^2 \right)}{P_s \gamma} \right)^{1/2} dA$$

$$Eq.2: \dot{m} = \int \rho u \ dA$$

$$Eq.3: Thrust_x = \int \left[\rho u_x{}^2 + \left(P_s - P_o \right) \right] dA$$

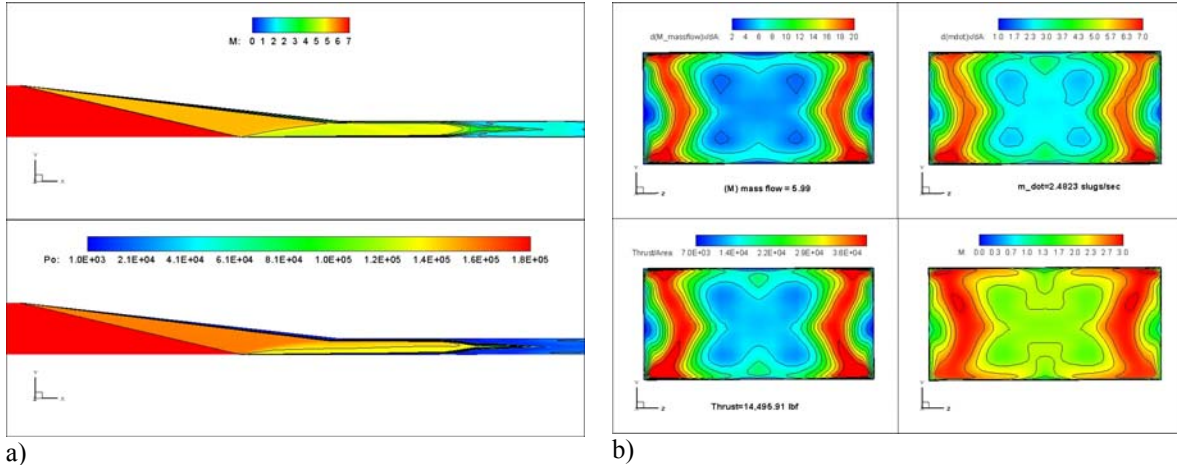$$Eq.4: MassAverageMachNumber = M\_massflow / \dot{m}_{ave}$$

6

Figure 5: Turbulent solutions for the rectangular inlet; a) Mach number (top) and total pressure (bottom) contours for the X-Y symmetry planes, and b) Mach mass-flow, mass flow rate, thrust and Mach contours at the 4th turn.

The equivalent analysis for the Jaws concept is presented in Figure 6, which illustrates the flow in the two symmetry planes (X-Z and X-Y) and six other cut planes. Again, the boundary layer growth and its interactions with the shocks significantly affect the downstream flow. Unlike in its rectangular counterpart, in the first two interactions the shock produced from the first ramp encounters a shock-shock interaction with its symmetric counterpart (Station II). These initial flow characteristics in the inlet direct the flow with fewer irregularities and smaller internal losses. The geometrical shape of Jaws provides some benefits at this section by having smaller wall surfaces in contact with the flow, which results in lesser boundary layer growth and overall friction drag (see 1st Ramp in Fig. 6).

In addition, this unique shape offers an irregular boundary profile that is more predominant on the very top and bottom walls in the first two turns (Fig. 1b), and afterward interacts with the second pair of shocks (see Station III). Further down from the 1st Ramp this shock- boundary layer interaction at the upper and lower walls of the inlet trips the flow into a more severe separation than what was observed on the Rectangular inlet, seen on the X-Y symmetry plane. At the 2nd Ramp the side walls of the inlet produce two vertical shock structures, one at each side; these effects are visible at the X-Z plane. On the 2nd Ramp, the boundary layer begins to turn more predominantly from side to side than from the top and bottom as seen in early stations. At the setting shown in Station IV, there is a second shock-shock interaction from the side walls (2nd Ramp), and the two vortices of flow separating from the top and bottom interact with the side compression waves. Stations V and VI confirm further development of the two vortices as they propagate downstream. Following these shock interactions the boundary layer growth on the upper and lower walls remains fairly constant while the fourth pair of shocks intersects off course from its design locations.
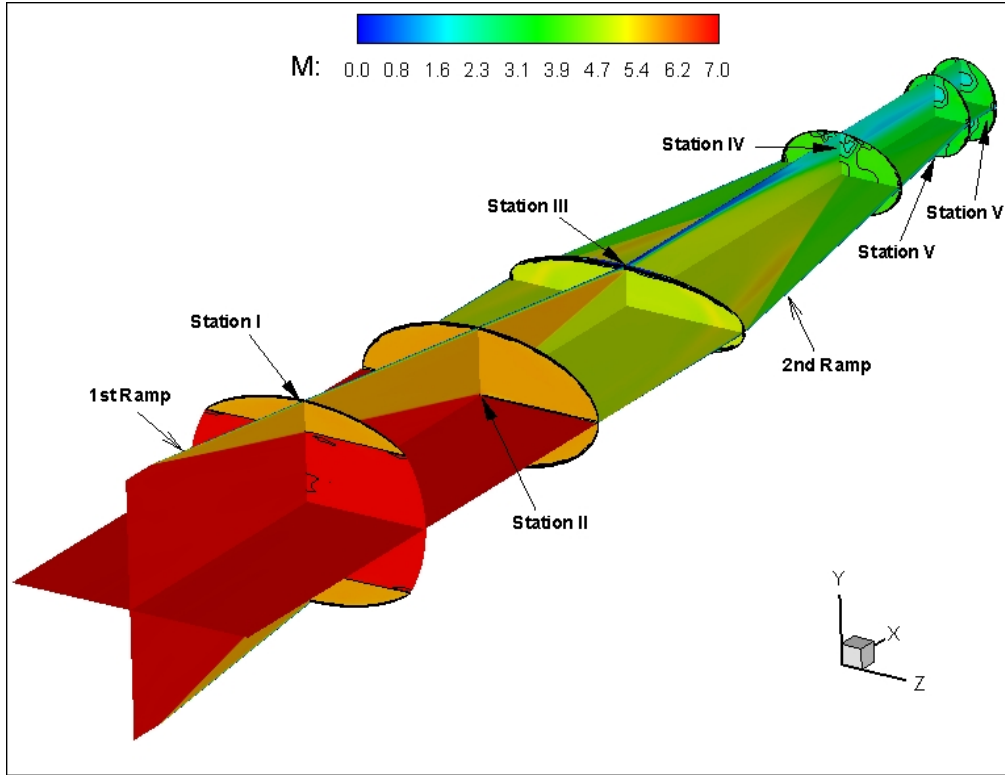
Figure 6: Turbulent solutions for Jaws, Mach Number contours at the symmetry planes (X-Z and X-Y), and six other cross sections in Jaws.

As shown earlier, Figure 7a-b shows Mach contours on the two planes at the center of the inlet at the $y_{ave}=(y_{max}-y_{min})/2$ and $z_{ave}=(z_{max}-z_{min})/2$, respectively, while Fig. 7c shows the irregularities of the flow at the exit section of the inlet on the 4th turn for different variables. At this location (see Station V in Fig. 6 as reference), the same four different parameters are employed for comparison with its counterpart as follows.
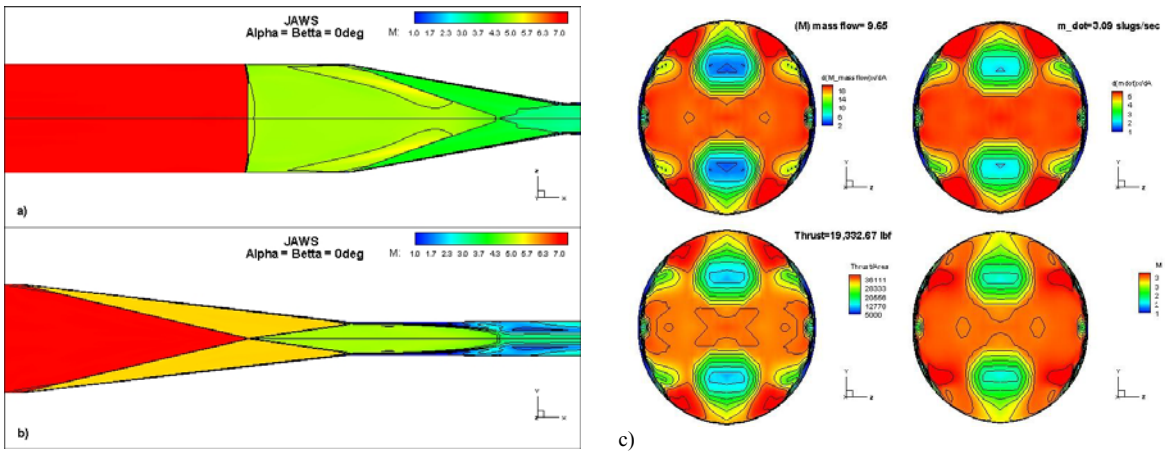

Figure 7: Turbulent solutions for Jaws; Mach Number contours for a) X-Z, b) X-Y symmetry planes, and c) Mach mass-flow, mass flow rate, thrust and Mach contours at the 4th turn.

The fourth equation is the most significant of all. This gives an average Mach number by the mean momentum at the inlet exit plane after the fourth turn; it represents a quantity of compressed air later chemically reacted downstream in the combustor. The thrust is the force acting per unit area at that plane due to two components: 1) pressure which demonstrates the pressure losses due to the turnings and boundary layer effects, providing a more complete picture that differentiates the effectiveness of the inlets,

8

and 2) the mass flow captured by the inlet. This can also be an indicator of the spillage through the lips if a freestream boundary condition is deployed at the exterior sides of the inlets as previously discussed.

Table 2: Baseline values employed for comparison between both inlets.			
Inlet Configuration	Mass-average Mach Number	Mass-flow rate slugs/sec *(kg/sec)*	Thrust lbf *(kN)*
Rectangular	2.41	2.48 (~36.18)	14.5_x10^3 (~64.54)
Jaws	3.12	3.09 (~45.08)	19.3_x10^3 (~85.90)

The following plot (Fig. 8) clearly shows the Mach number of the center line at Jaws compared to the middle line through the rectangular inlet a short distance away from the boundary layer (~2.5 cm away from the bottom wall). The entropy gain of both inlets, as well as their Mach numbers, match upon reaching the isolator (after the 4th turn). The Mach number drops for the rectangular inlet happen earlier and at a greater rate than in the Jaws inlet. This effect is due to their ramp locations. As explained earlier, the particular geometrical shape of Jaws causes the flow to detach during the first ramp from the top and bottom, forming two vortices after the third turn. This effect propagates into some downstream disturbances to the center line, as can be observed below (13.5ft to 15.5ft).
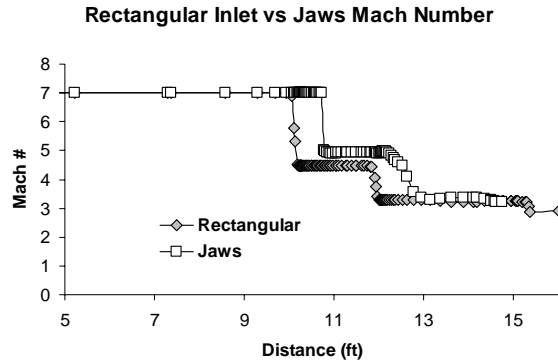
Rectangular Inlet vs Jaws Mach Number

Figure 8: Mach Number vs streamwise distance at the center line of both inlets.

Chemical Mechanisms and Models
($C_{12}H_{23}$- Air; Equations for the dispersed phase)

The liquid phase is simulated by solving Lagrangian equations of motion and transport for the life histories of a statistically (probability function) significant sample of individual droplets. This involves dividing the droplets into *n* groups (defined by position, velocity, temperature and diameter) at the fuel nozzle exit and then computing their subsequent trajectories in the flow. The liquid fuel is assumed to enter the combustor as a fully atomized spray comprised of spherical droplets. The present model does not account for the effects due to droplet breakup and coalescence which might be significant in a dense spray situation. The Lagrangian equations governing the droplet motion are:

$$Eq:1 \qquad \frac{dx_p}{dt} = u_{pi}$$

$$Eq:2 \qquad \frac{dy_p}{dt} = v_{pi}$$

$$Eq:3 \qquad \frac{du_p}{dt} = \frac{3}{16} \frac{C_D \mu_g \operatorname{Re}_p}{\rho_p r_p^{\,2}} \left(u_g - u_p \right)_i$$

$$Eq:4 \qquad \frac{dv_p}{dt} = \frac{3}{16} \frac{C_D \mu_g \operatorname{Re}_p}{\rho_p r_p^{\,2}} \left(v_g - v_p \right)_j$$

9

Where the Reynolds number and drag coefficient are:

$$Eq:5 \qquad \mathrm{Re}_p = 2\frac{r_p \rho_g}{\mu_g}\left[\left(u_g - u_p\right)^2 + \left(v_g - v_p\right)^2\right]_i^{1/2}$$

$$Eq:6 \qquad C_D = \frac{24}{\mathrm{Re}_p}\left(1 + \frac{\mathrm{Re}_p^{2/3}}{6}\right)$$

$$for \qquad \mathrm{Re}_p \prec 1000; \qquad and$$

$$C_D = 0.44$$

$$for \qquad \mathrm{Re}_p \succ 1000$$

The subscript g represents the gas-phase quantities and p represents the liquid-phase (or "particle") quantities. Equations 1 and 2 are integrated with a second-order Runge-Kutta scheme to calculate the new droplet positions, while Equations 3 and 4 update the droplet velocities at the new droplet locations. The mass and heat transfer coefficients for a single isolated spherical droplet are given by:

$$Eq:7 \qquad \frac{m_p^{''} d_p}{\rho D_f} = 2N_s \, \ln(1+B)_i$$

$$Eq:8 \qquad \frac{h d_p}{k} = \frac{2N_p \, \ln(1+B)^{Le^{-1}}}{\left[(1+B)^{Le^{-1}} - 1\right]_i}$$

where,

$$Eq:9 \qquad N_s = 1 + \frac{0.276\,\mathrm{Re}_p^{1/2}\,\mathrm{Pr}^{1/3}}{\left[1 + \frac{1.232}{\mathrm{Re}_p\,\mathrm{Pr}^{4/3}}\right]^{1/2}}$$

$$Eq:10 \qquad N_p = 1 + \frac{0.276\,\mathrm{Re}_p^{1/2}\,\mathrm{Sc}^{1/3}}{\left[1 + \frac{1.232}{\mathrm{Re}_p\,\mathrm{Sc}^{4/3}}\right]^{1/2}}$$

A large-eddy simulation model (LES) for spray combustion was utilized to investigate the unsteadiness of a scramjet combustor. LES is intermediate in complexity between conventional Reynolds-averaged Navier-Stokes (RANS) and computationally expensive direct numerical simulation (DNS) methods. RANS approaches are not sufficiently accurate for predicting many important reacting flows while DNS is too costly for practical applications. However, in LES, the large energy-containing scales are resolved and computed directly (as in DNS) and only the smaller subgrid scales, which tend to be more homogeneous and universal, are modeled (as in RANS) making the approach a very promising computational tool. LES has the potential to be both sufficiently accurate and efficient for the prediction of turbulent reacting flows and is currently of great interest to the combustion research community. Nevertheless, several issues must first be resolved if LES is to be used for practical computations. These include the influence of filtering and discretization errors, subgrid-scale modeling for the unresolved turbulence and chemistry, effective numerical solution strategies, and simulation requirements for LES of compressible wall-layers.

Scales larger than the grid size are computed using a time- and space- accurate scheme, while the unresolved smaller scales are modeled by LES. Closure of momentum and energy transport equations is

accomplished with a sub-grid eddy viscosity model, since the small scales mainly provide a dissipative mechanism for the turbulence energy transfer from the large scales to the small scales. Here, a localized dynamic model for the sub-grid kinetic energy is used for momentum closure. It has been shown in the past that for proper implementation of the sub-grid combustion model, information on the sub-grid turbulence intensity is needed. Therefore, the present sub-grid kinetic energy model provides not only a closure for the momentum transport equations but also yields a natural and accurate estimate for sub-grid turbulence intensity. Closure of species transport and the reaction-diffusion processes occurring at the small-scales is carried out using the sub-grid combustion model based on the linear-eddy model (LEM) that has already proven capable of capturing quantitatively the structure and propagation characteristics of turbulent premixed flames over a wide range of operational parameters.

The mean steady calculations assume finite-rate chemical kinetics for 13 species ($C_{12}H_{23}$, C_2H_2, CO_2, CO, OH, O_2, O, H_2, H, H_2O, NO, N and N_2) and 20 reactions pertinent to JP8- Oxygen, and Nitrogen-based combustion products. The reaction set is shown as follows (Table 2):

Table 2: Chemical reactions of the reduced reaction mechanism

React. 1	$2C_{12}H_{23} => 12C_2H_2 + 11H_2$	React. 11	$H + OH + M => H_2O + M$
React. 2	$C_2H_2 + O_2 => 2CO + H_2$	React. 12	$H + O + M => OH + M$
React. 3	$CO + O + M => CO_2 + M$	React. 13	$2O + M => O_2 + M$
React. 4	$CO + O_2 => CO_2 + O$	React. 14	$N + NO => N_2 + O$
React. 5	$CO + OH => CO_2 + H$	React. 15	$N + O_2 => NO + O$
React. 6	$OH + H_2 => H_2O + H$	React. 16	$N + OH => NO + H$
React. 7	$O + OH => O_2 + H$	React. 17	$H_2 + O_2 => 2OH$
React. 8	$O + H_2 => OH + H$	React. 18	$2H + H_2 => 2H_2$
React. 9	$2OH => O + H_2O$	React. 19	$2H + H_2O => H_2 + H_2O$
React. 10	$2H + M => H_2 + M$	React. 20	$2H + CO_2 => H_2 + CO_2$

For both combustors simulations, the sub-grid chemistry is described with a 2-step assumed PDF method. The PDF is a 2-dimensional function of the mixture fraction and progress variable (fuel mass fraction), where these variables are assumed to be independent of each other. Top-hat and tri-delta PDF shapes are assumed for the mixture fraction and reaction progress variables, respectively, since they are relatively inexpensive to compute and have given reasonable results in previous combustor calculations. Filtered transport equations for the mean and variance of the mixture fraction and reaction progress are solved. The sub-grid reaction rate is obtained by integrating the instantaneous fuel reaction rate over the PDF. Source terms in the transport equations for the mixture fraction and progress variable variance are obtained from the sub-grid turbulent kinetic energy and dissipation rate.

Combustors Results (Cases 3$_{a-b}$)

As previously explored by the authors and other researchers, downstream sections of the inlets show distortions due to the flow interactions. These interactions can yield a region of enhanced turbulence in the isolator, shown to have a significant effect on the combustor, since a better mixing of air and fuel can significantly augment the chemical reactions and improve the overall efficiency of the hypersonic propulsion system.[x and xi] It is important to understand: 1) the three-dimensional interplay between viscous

and inviscid interactions including shock -boundary layer and shock-shock interactions in the inlet; as well as 2) the positive effects due to combustion of the reacting stoichiometric fuel-air mixture described above. [v, xii and xiii]

Liquid jet fuel is introduced into the engine through rounded injectors positioned perpendicularly into the air flow upstream of the combustor. For the rectangular inlet, injection occurs from the top and bottom walls (Case 3a). In this case, a symmetrical 3D section with jet fuel was injected by two circular injectors, mounted in the combustion chamber of the duct at different locations lengthwise and positioned to interlace each other in the spanwise direction. The bottom injector is upstream while the top injector is downstream. In addition, a TVC is positioned on the top surface, immediately after the second and last row of injectors with the noted dimensions (length equal to three times the height; and 30° ramp). These sections were designed by selecting optimal features from other common designs,[9] coupled with CFD to determine a better combination of features (see Fig. 1).

Figures 9 and 10 show the complexity of reacting flow patterns. Figure 9 illustrates the atomization of the liquid fuel particles as they emanate from the top and bottom, mixing with the captured air, recirculating inside the TVC and subsequently dissipating/burning downstream.
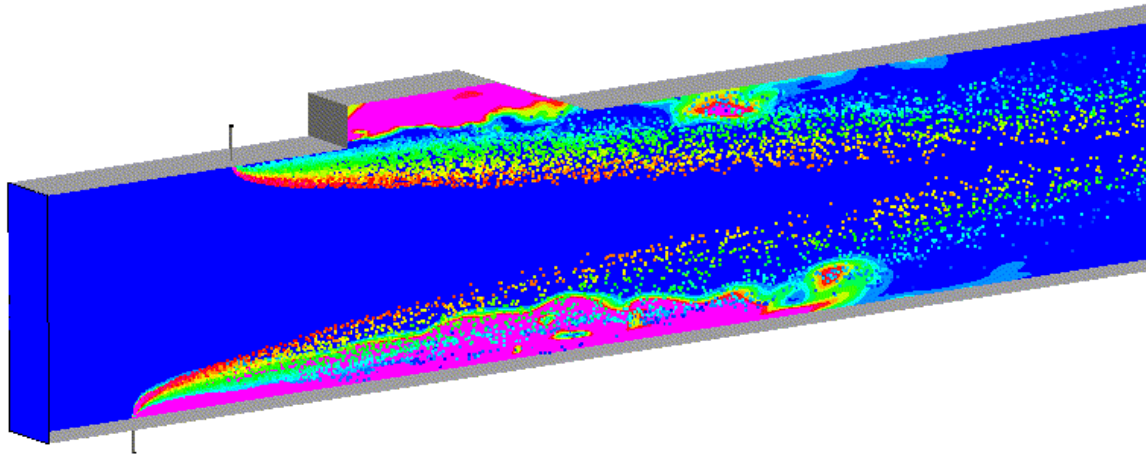

Fig. 9: Multi-phase simulation of the atomization of the liquid fuel droplets inside the rectangular combustor as they exit the top and bottom injectors, mixing with air and burning.

Figures 10a-b depicts the Mach number and temperature contours of the Rectangular combustor configuration at the symmetry plane (k_{ave}). A clear picture of the jet penetration and complete combustion process appears when these are considered together with those in 11a-b, which exhibit mass concentrations of various species. The mixing and jet fuel penetration on the computed rectangular combustor geometry is very effective; combustion efficiency is 81%.
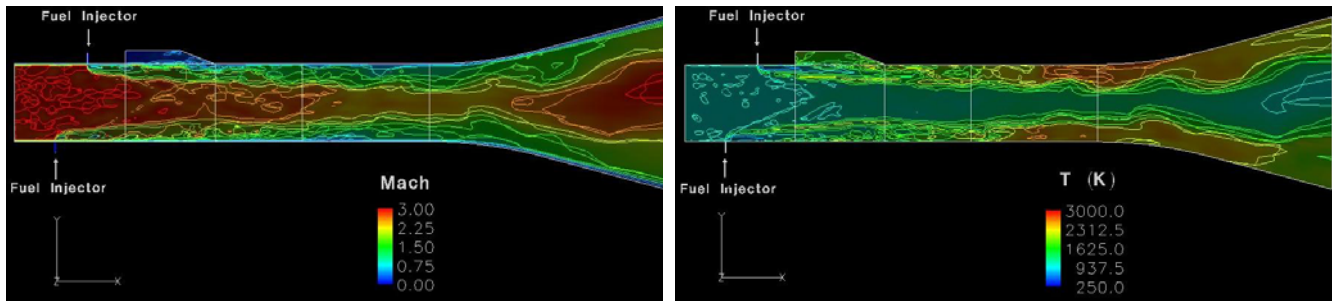

a)   b)

Fig. 10: a) Mach Number and b) Temperature contours at XY-planes.

Figure 11a (top and bottom) shows the mass fractions for the reactants (O_2 present in the captured air and hydrocarbon fuel); while Figure 11b (top and bottom) illustrates the main products CO_2 and H_2O at the symmetry plane (k_{min}). The mole fraction of the unburned fuel was further reduced by sheltering the second injection after the first one and creating additional eddies towards the TVC. This following figure shows the burning at the higher levels of water and carbon dioxide mass fractions (seen in red).
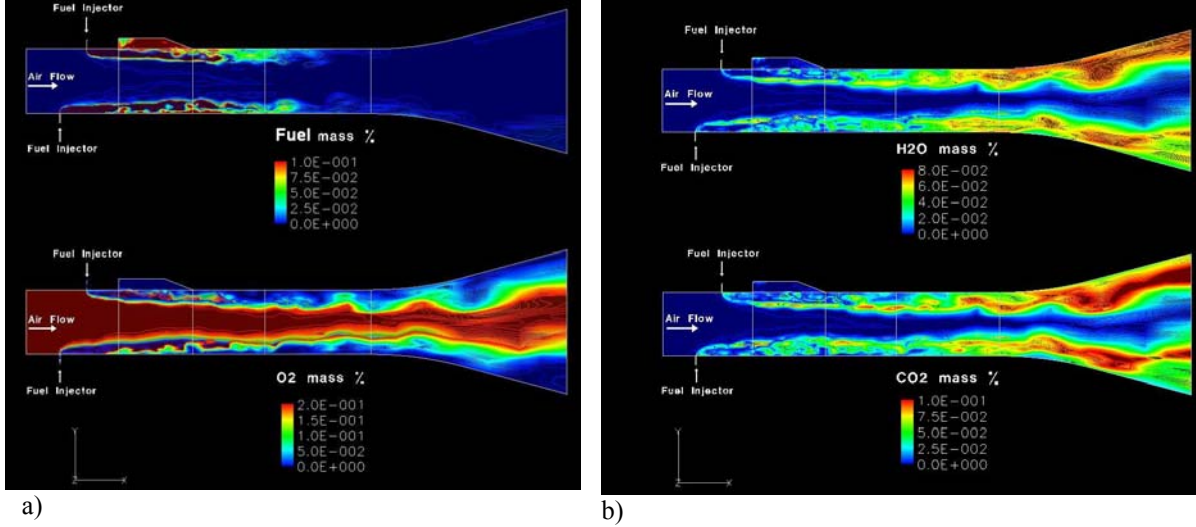

a)   b)

Fig. 11: a) Fuel (C_7H_{16}, top) and Oxygen (O_2, bottom), and b) Water (H_2O, top) and Carbon dioxide (CO_2, bottom) mass fraction contours at the symmetry plane (k_{ave}).

In the case of Jaws, the same total number and size of injectors are positioned at equal distance around the combustor. In this analysis, only an axis-symmetrical slide of the combustor geometry was computed. Figure 12a shows the temperature surface of the liquid fuel droplets, the Mach (top) and pressure (bottom) contours of Jaws' combustor configuration at the symmetry plane (k_{min}). The jet penetration and complete combustion process is shown in Fig. 12b, which displays molar concentrations of various species. The cavity recirculation zone transports some of the hot combustion products back toward the combustor face (along the cavity's back wall) and ignites the incoming fuel and air as it is mixed in the combustion chamber. The mean temperature in the cavity is close to the stagnation temperature of incoming air flow. These recirculation zones form an exceptionally stable combustion region and are aerodynamically stable over a wide range of fuel-air ratios and inlet temperatures and pressures. Furthermore, the products from the fuel-rich-zone remain within the cavity (see Fig. 12b) and drive a stable combustion system. Mixing can be seen within the shear layer above the cavity as shown in Figure 12a-b. The vortex diameter is about the size of cavity depth. By comparing the injected fuel to the burned mole fraction values at the exit, it is estimated that the combustion efficiency or burned fuel is about 70%.
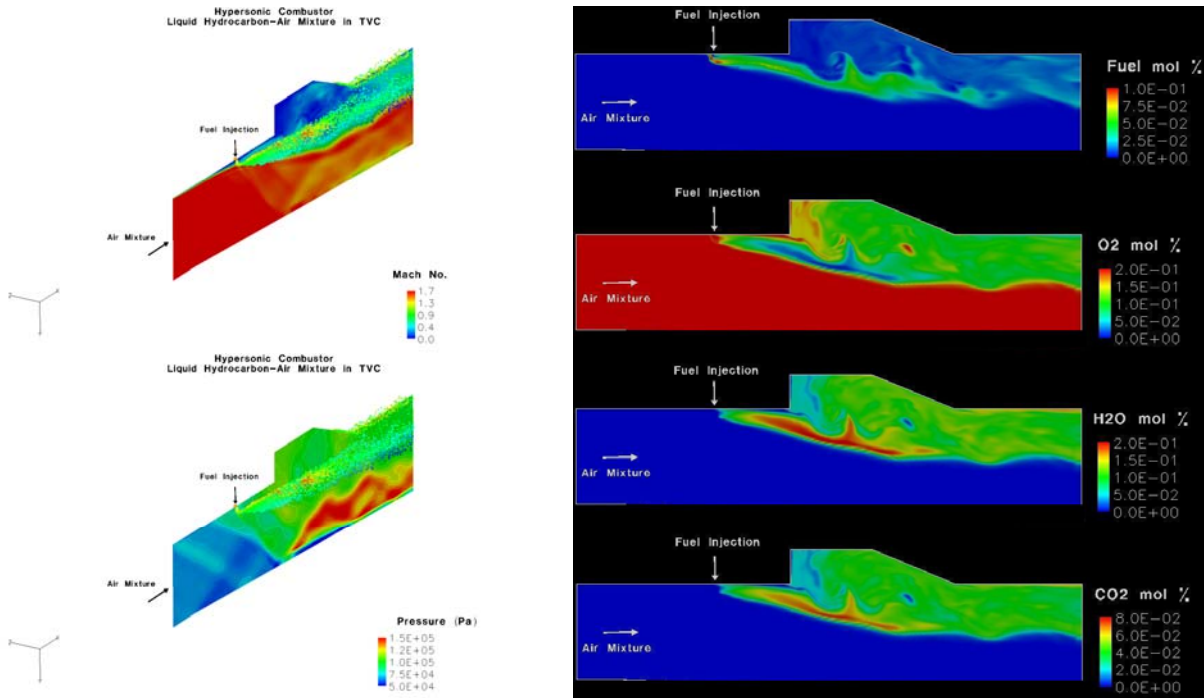
Fig. 12: a) Mach Number (top) and pressure contours (bottom) at the axis-symmetry plane, center at the injector in the Jaws' combustor. b) Fuel (JP8), Water, Oxygen and Nitrogen mole fractions (from top to bottom).

Conclusion

Numerical efforts to investigate flows in two different hypersonic inlets are presented. Both devices are designed to operate at Mach 7 and dynamic pressures of 1,500 psf. The airflow is compressed through four compression corners, in mutually orthogonal planes, thus reducing the Mach number while raising the temperature to favorable conditions for the combustor. A combination of GASP and GPACT codes is employed to solve the Navier-Stokes equations together with a *k-w* model (inlet) and LES chemistry to characterize the effects of turbulence and combustion (combustor), respectively. Two configurations, Jaws and a rectangular inlet are explored. Shock-shock and shock-boundary layer interactions are shown to have a significant effect on the flow due to their profiles. These interactions enhance distortion as a result of separation and vertical flow formation. In addition, they can hinder combustor mixing and overall efficiency of the engine.

A GPACT solution model with spray is used to solve Navier-Stokes equations with multi-phase chemically reacting flow, in strong conservative form. Complex aerodynamic flow interactions occurring in the cavity zone are evident, and effectiveness in terms of mixing is summarized. The rectangular inlet injector configuration is observed to yield relatively higher combustion efficiency than its counterpart. However, Jaws offers less drag and captures about 20 percent more air than the rectangular inlet. This translates into a 24.87% greater thrust and 22.75 % greater Mach numbers at the combustor inlet. The effectiveness of complex aerodynamic flow interactions are characterized in terms of Mach-mass-flow averaging, mass flow rate and thrust measured as pressure losses.[xiv]

References

i Chase, R L, Tang, M. H., "A history of the NASP Program from the formation of the Joint Program Office to the termination of the HySTP Scramjet Performance Demonstration Program." 6th International Aerospace Planes and Hypersonics Technologies Conference, AIAA Paper 1995-6031, April 1995.

ii Fry, Ronald S.; "A Century of Ramjet Propulsion Technology Evolution," Journal of Propulsion and Power, Vol. 20, No. 1, January-February 2004.

iii Heiser, William H.; and Pratt, Davit T., "Hypersonic Airbreathing Propulsion" AIAA, Education Series; Washington, DC, 1994, pp. 2-27.

iv Baurle, R. A., Mathur, T., Gruber, M. R., and Jackson, K. R. "A Numerical and Experimental Investigation of a Scramjet Combustor for Hypersonic Missile Applications." AIAA Paper 98-3121, July 1998.

v Gruber, M., Donbar, J., Donaldson, W., Jackson, T., Mathur, T., Eklund, D., and Billig, F. "Performance of an Aerodynamic Ramp Fuel Injector in a Scramjet Combustor." presented at 36th JANNAF Combustion Subcommittee/Airbreathing Propulsion Subcommittee Meeting, October 1999.

vi Malo-Molina, Faure J., Gaitonde, Datta V., and Ebrahimi, Houshang B., "Numerical Investigation of a 3-D Chemically Reacting Scramjet Engine at High Altitudes Using JP8 - Air Mixtures." 43rd AIAA Aerospace Sciences Meeting & Exhibit, AIAA Paper 2005-1435, January 2005.

vii Wilcox, David C. (DCW Industries, Inc., La Canada, CA), "More Advanced Applications of the Multiscale Model for Turbulent Flows." 26th AIAA Aerospace Sciences Meeting, AIAA Paper 1988-220, January 1988.

viii Baurle, R. A., and Eklund, D.R., "Analysis of Dual-Mode Hydrocarbon Scramjet Operation at Mach 4-6.5," Journal of Propulsion and Power, Vol. 18, No. 5, 2002, pp. 990-1002.

ix Gaitonde, Datta V., "Three Dimensional Flow-Through Scramjet Simulation with MGD Energy-Bypass," 42nd AIAA Aerospace Sciences Meeting, AIAA Paper 2003-0172, January 2003.

x Goyne, C. P., McDaniel J. C., Quagliaroli, T. M., Krauss, R. H., and Day, S. W., "Dual-Mode Combustion of Hydrogen in a Mach 5 Continuous-Flow Facility," Journal of Propulsion and Power, Vol. 17, No. 6, 2001, pp. 1313–1318.

xi Ebrahimi, H. B. "Numerical Simulation of Transient Jet-Interaction Phenomenology in a Supersonic Freestream." AIAA Journal of Spacecraft and Rockets, Vol. 37, No. 6, November and December 2000.

xii Gruber, M., Jackson, K., Jackson, T., and Mathur, T. "Investigations of Shock Trains in Rectangular Ducts." JANNAF 35th Joint APS Meeting, Paper Number 4D-03, December 1998.

xiii Mathur, T., Lin, K.-C., Kennedy, P. J., Gruber, M. R., Donbar, J. M., Donaldson, W. A., Jackson, T. A., Smith, C. R., and Billig, F. S. "Liquid JP-7 Combustion in a Scramjet Combustor." presented at 36th JANNAF Combustion Subcommittee/Airbreathing Propulsion Subcommittee Meeting, October 1999.

xiii Malo-Molina, Faure J., Gaitonde, Datta V., and Ebrahimi, Houshang B., "Numerical Investigation of an Innovative Inward Turning Inlet." 17th AIAA Computational Fluid Dynamics Conference, AIAA Paper 2005-4871, 6-9 June 2005; Toronto, Ontario, Canada.